

6. ANTARCTICA AND THE SOUTHERN OCEAN—T. Scambos and S. Stammerjohn, Eds.

a. Overview—T. Scambos and S. Stammerjohn

The year 2018 was marked by extreme seasonal and regional climate anomalies in Antarctica and across the Southern Ocean, expressed by episodes of record high temperatures on the high Antarctic Plateau and record low sea ice extents, most notably in the Weddell and Ross Seas. For the Antarctic continent as a whole, 2018 was warmer than average, particularly near the South Pole ($\sim 3^\circ\text{C}$ above the 1981–2010 reference period), Dronning Maud Land (1° to 2°C above average), and the Ross Ice Shelf and Ross Sea (also 1° to 2°C above average). In contrast, and despite conducive conditions for its formation, the ozone hole at its maximum extent was near the mean for 2000–18, likely due to an ongoing slow decline in stratospheric chlorine monoxide (ClO) concentration. This section summarizes the year's progression of notable climate-related events for the southern continent and the polar ocean surrounding it. Locations discussed in this chapter are shown in Fig. 6.1.

Early in 2018 (January–February), a localized but strong low-pressure anomaly spanning the southeast Pacific to southwest Atlantic sectors produced highly contrasting regional temperature anomalies across the continent—notably, near-record low temperatures over West Antarctica and record high temperatures over the East Antarctic Plateau. Very low summer sea ice extent in the Ross and Weddell Seas in 2018 (following on from the anomalously low spring 2017 pattern) led to the second lowest Antarctic summer minimum extent on record. This was accompanied by high SSTs in the Ross and Weddell Seas, with the latter also showing high coastal precipitation. Summer sea ice extent in the western Bellingshausen Sea and Amundsen Sea sectors was higher than typical, and was associated with low SSTs and low coastal precipitation. Cool conditions in this sector also contributed to a low ice sheet melt season overall for 2017/18. This low-melt year continues a trend, now spanning from the 1978/79 to 2017/18 seasons, of reduced summer melting that is statistically significant ($p < 0.05$).

From austral autumn to early winter (March–June), low-pressure

anomalies continued to persist over the Antarctic Peninsula. In conjunction with negative southern annular mode (SAM) index values that contrasted with positive values both before and after this period, positive pressure anomalies emerged over the continental interior, producing widespread high temperatures across the ice sheet interior, with record highs observed at several continental stations (Relay Station AWS, Amundsen–Scott South Pole Station). Circumpolar sea ice extent remained well below average throughout the year, as has been the case since September 2016.

In spring (October), a strong but short-lived wave-three pattern developed, producing strong regional contrasts in temperature and pressure anomalies. At the same time, the stratospheric vortex intensified, but due to decreasing CIO in the stratosphere, the cold and intensified polar vortex resulted in only a near-average ozone hole area.

Late in the year (November–December), the atmospheric circulation was characterized by a wave-two pattern, leading to more record high temperatures on the high Antarctic Plateau (Amundsen–Scott reached -23.3°C ; Relay Station AWS reported -25.7°C in December) and daily records of low circumpolar sea ice extent, particularly in late December. The annual $P - E$ anomaly pattern was also marked by a wave-two pattern with anomalously low precipitation in coastal

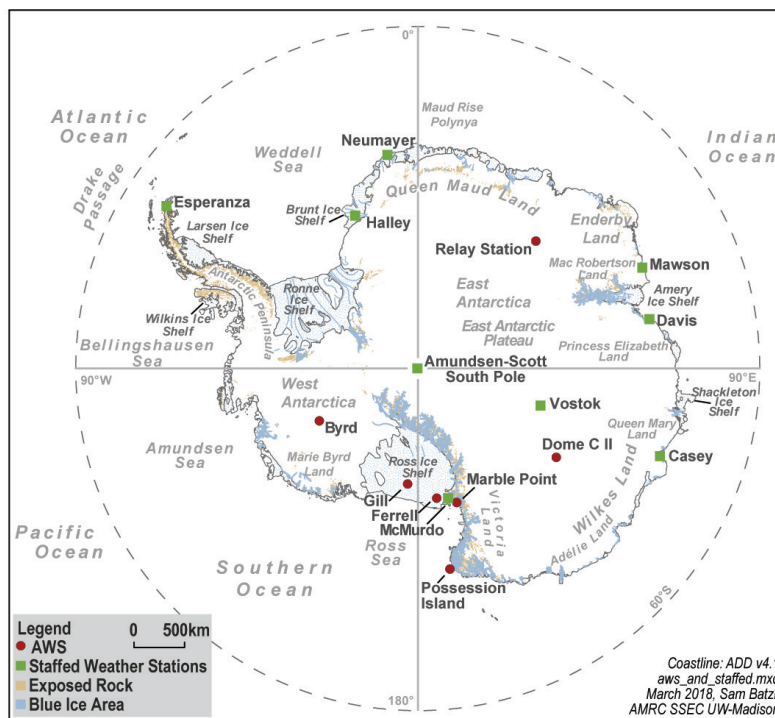


FIG. 6.1. Map of stations, locations, and other regions discussed in this chapter, and the locations of weather stations.

West Antarctica and coastal East Antarctica (~170°E to ~80°W, ~80°E to ~140°E, respectively); elsewhere, precipitation was generally above average, particularly in the coastal Weddell sector.

b. Atmospheric circulation and surface observations—

K. R. Clem, S. Barreira, R. L. Fogt, S. Colwell, L. M. Keller, and M. A. Lazzara.

Atmospheric circulation anomalies contributed to several record-breaking weather conditions observed in 2018. Atmospheric pressure and temperature anomalies were investigated using ERA-Interim (Dee et al. 2011), which performs with greater skill over the high southern latitudes than other modern global reanalyses (Bracegirdle and Marshall 2012), although the results shown here are consistent with the other reanalyses. Figure 6.2 shows the monthly geopotential height (Fig. 6.2a) and temperature (Fig. 6.2b) anomalies averaged over the polar cap (60°–90°S) and the monthly circumpolar zonal wind (Fig. 6.2c) anomalies averaged over 50°–70°S. The year was split into five periods characterized by distinctive general climate patterns: January–February, March–June, July–September, October, and November–December. The normalized surface pressure and temperature anomalies for each period are shown in Fig. 6.3. Figure 6.4 shows monthly pressure and temperature anomalies for four staffed weather stations (Amundsen–Scott, Esperanza, Halley, and Mawson) and two automatic weather stations (AWS; Marble Point AWS and Relay Station AWS). The station anomalies provide an indication of the surface weather that contributed to the patterns shown in Fig. 6.3.

The year began with below-average pressure over the continent during January and February (Fig. 6.2a) and a strong low-pressure anomaly over the South Pacific and Amundsen and Bellingshausen Seas that was 2–3 standard deviations and 9–12 hPa (not shown) below the climatological average (Fig. 6.3a). Halley station tied its record lowest

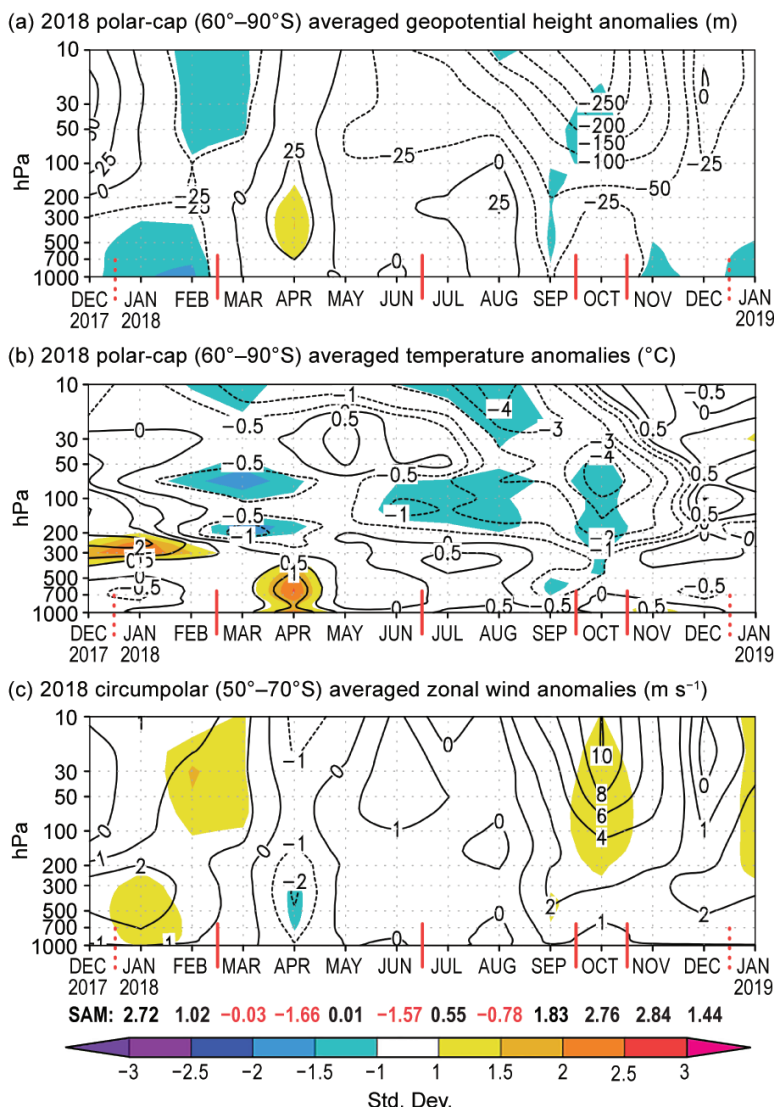


FIG. 6.2. Area-averaged (weighted by cosine of latitude) monthly anomalies over the southern polar region in 2018 relative to 1981–2010: (a) polar cap (60°–90°S) averaged geopotential height anomalies (contour interval is 50 m with additional contour at ± 25 m); (b) polar cap averaged temperature anomalies (contour interval is 1°C with additional contour at $\pm 0.5^\circ\text{C}$); (c) circumpolar (50°–70°S) averaged zonal wind anomalies (contour interval is 2 m s⁻¹ with additional contour at ± 1 m s⁻¹). Shading depicts std. dev. of monthly anomalies from the 1981–2010 climatological average as indicated by color bar at bottom. (Source: ERA-Interim reanalysis.) Red vertical bars indicate the five climate periods used for compositing in Fig. 6.3; the dashed lines near Dec 2017 and Dec 2018 indicate circulation anomalies wrapping around the calendar year. Values from the Marshall (2003) SAM index are shown below (c) in black (positive values) and red (negative values).

pressure value for February, which is more than 7 hPa below its February climatological average (Fig. 6.4c). January–February surface air temperatures over central West Antarctica and the Weddell Sea were 2–3 standard deviations below normal. A localized but strong positive temperature anomaly (2 standard

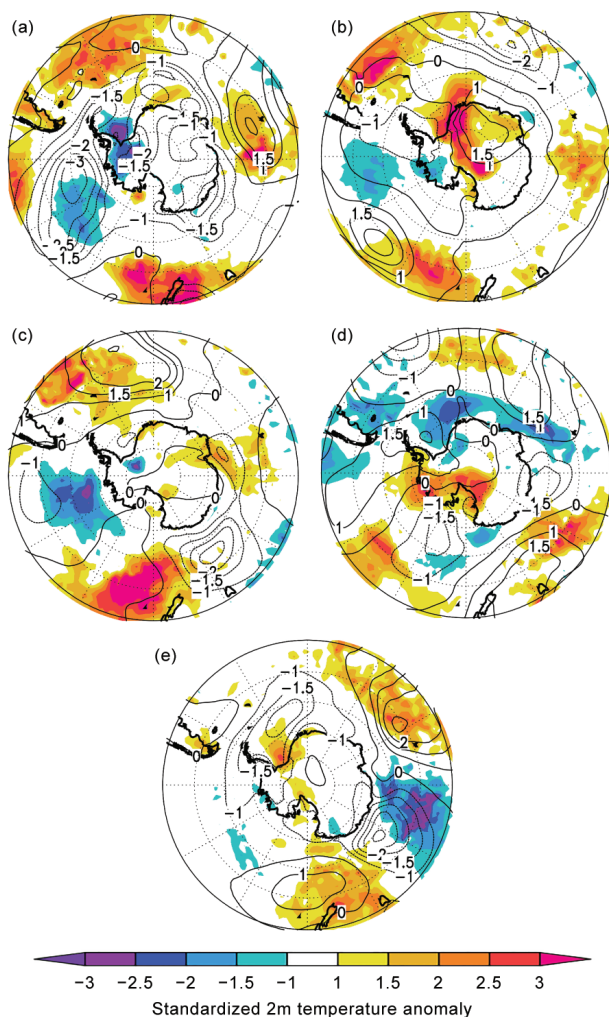


FIG. 6.3. Standardized surface pressure (contours) and 2-m temperature anomalies (shaded) relative to 1981–2010 for (a) Jan–Feb 2018; (b) Mar–Jun 2018; (c) Jul–Sep 2018; (d) Oct 2018; (e) Nov–Dec 2018. Contour interval is 0.5 std. dev. of surface pressure anomalies with the ± 0.5 contour omitted. Shading represents std. dev. of 2-m temperature anomalies. (Source: ERA-Interim reanalysis.)

deviations) was observed over the polar cap at the 200–300 hPa level during January and February (Fig. 6.2b). This included positive temperature anomalies observed at the highest points of the Antarctic Plateau; Relay Station AWS tied its record high monthly mean temperature for January (-26.1°C) and observed a new record high monthly mean temperature of -35.4°C for February (Fig. 6.4f). Elsewhere around the continent, temperatures were generally near normal for January–February. The negative pressure anomalies over the polar cap were accompanied by positive circumpolar zonal wind anomalies that were $1\text{--}2\text{ m s}^{-1}$, or about 1 standard deviation, above the January climatology (Fig. 6.2c). Positive values of the

southern annular mode (SAM) index were observed in both months.

With the development of a strong positive pressure anomaly (>1.5 standard deviations) over the Antarctic Plateau, atmospheric circulation underwent a marked transition in March that persisted through June. Negative pressure anomalies previously present in the South Pacific region of the Southern Ocean developed over the Antarctic Peninsula (Fig. 6.3b). As a whole, the polar cap experienced the most widespread positive pressure and temperature anomalies during April (Figs. 6.2a–b), and the circumpolar westerlies were $1\text{--}2\text{ m s}^{-1}$ (1 standard deviation) below normal (Fig. 6.2c), concurrent with the year’s most negative SAM index value. Through thermal advection, the positive pressure anomaly over the Plateau, combined with the negative pressure anomaly over the Peninsula, produced a narrow band of strong, positive temperature anomalies (>3 standard deviations) that extended from Halley Station ($4^{\circ}\text{--}6^{\circ}\text{C}$ above climatology from March–June) to Relay Station AWS and Amundsen–Scott. Amundsen–Scott Station and Relay Station AWS observed temperatures more than 6°C above average during May and June. Relay Station AWS set a new record high temperature in May (-50.1°C). Both Relay Station AWS and Amundsen–Scott Station tied their previous record high temperatures for June. On the Ross Ice Shelf, Marble Point AWS was $+4^{\circ}\text{C}$ above normal for June; in the Ross Sea, Possession Island AWS observed a record high temperature (-15.4°C) in June.

From July through September, temperatures and pressures over the continent were generally near average, but there were some strong month-to-month variations in temperature and pressure—particularly at Marble Point AWS and Amundsen–Scott Station. The most noteworthy and persistent feature was a strong positive pressure anomaly (>2 standard deviations) over the South Atlantic and a negative pressure anomaly (>2 standard deviations) south of Australia that extended westward and poleward to the Amery Ice Shelf (Fig. 6.3c). The latter, a cyclonic anomaly, produced positive temperature anomalies of $2^{\circ}\text{--}3^{\circ}\text{C}$ (not shown), or 1–2 standard deviations (Fig. 6.3c), during July–September across the Amery Ice Shelf and the adjacent coast; during August, Mawson set a new record high monthly temperature of -12.8°C , which is $+6^{\circ}\text{C}$ above its climatological average (Fig. 6.4d). Also, on the Plateau during August, Relay Station AWS observed a record high monthly mean temperature of -50.4°C , nearly $+8^{\circ}\text{C}$ above its climatological value for that month.

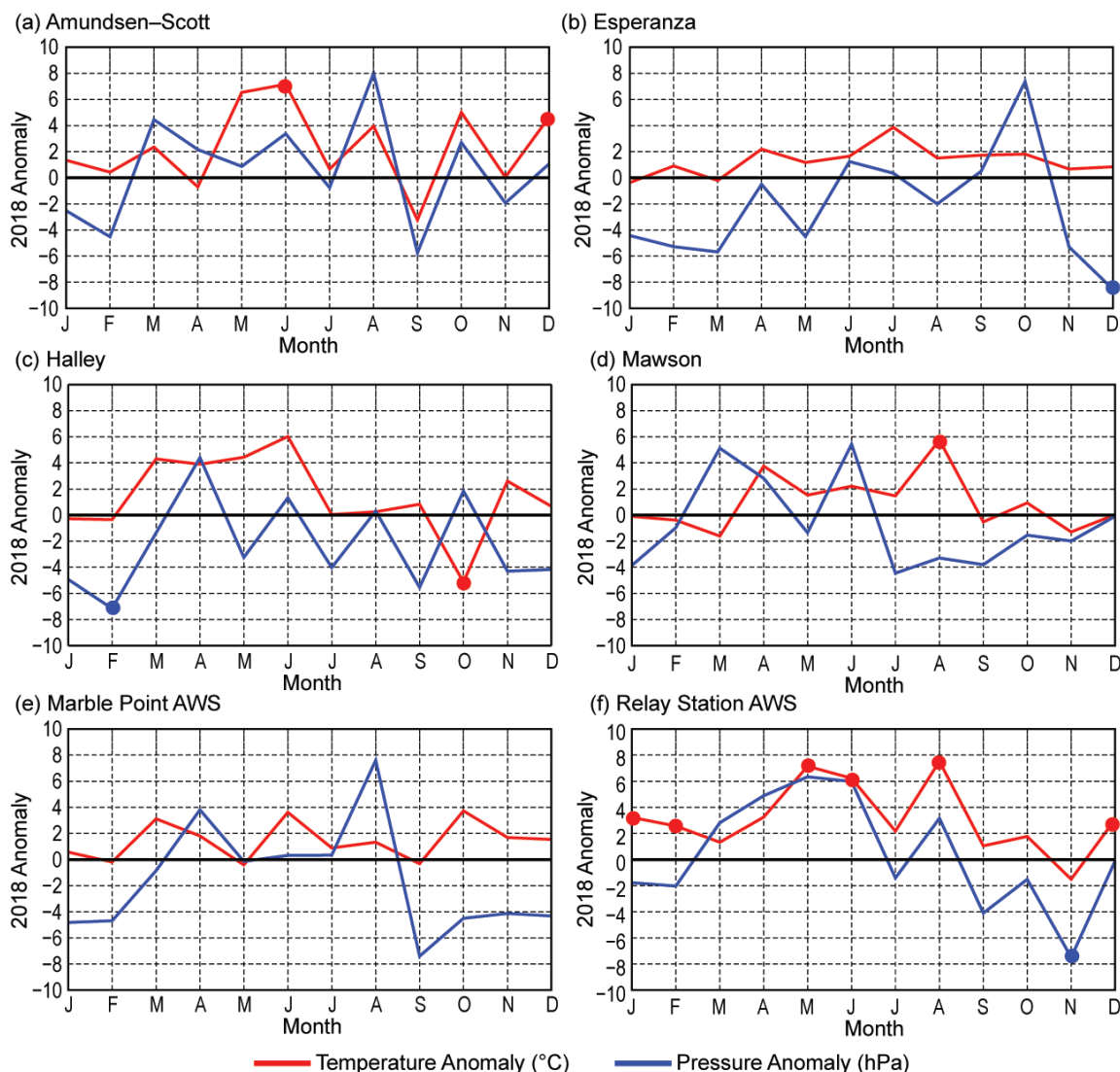


Fig. 6.4. Monthly Antarctic climate anomalies during 2018 at six representative stations [four staffed (a)–(d), and two automatic (e)–(f)]. Anomalies for temperature (°C) are shown in red and MSLP/surface pressure (hPa) are shown in blue, with filled circles denoting record or tied record anomalies for a given month at each station in 2018. All anomalies are based on differences from the monthly 1981–2010 averages except for Relay Station, which is based on monthly 1993–2017 averages. Observational data used to calculate record values start in 1957 for Amundsen–Scott and Halley, 1945 for Esperanza, 1954 for Mawson, 1980 for Marble Point AWS, and 1995 for Relay Station AWS.

In October, a strong but short-lived wave-three pattern developed with three anomalous ridges and troughs between 40°S and 60°S (Fig. 6.3d). There was a negative pressure anomaly in the Ross Sea and a positive pressure anomaly over the Peninsula and Weddell Sea region. Esperanza Station recorded a positive monthly pressure anomaly of more than 7 hPa (Fig. 6.4b). This regional circulation pattern produced strong warming across the western Antarctic Peninsula, Amundsen Sea, Marie Byrd Land, and the Ross Ice Shelf (Fig. 6.3d), including a +5°C anomaly at Amundsen–Scott and a +4°C anomaly at

Marble Point AWS (Figs. 6.4a,e). In the Weddell Sea, on the colder eastern side of the anticyclone, Halley Station set a new record low monthly temperature of –25.1°C during October. The stratospheric vortex also intensified during October, as a negative pressure and temperature anomaly propagated downward to ~30–100 hPa (Figs. 6.2 a,b). Stratospheric westerlies above ~100 hPa were 4–10 m s^{–1} (1 standard deviation) above average during October (Fig. 6.2c).

The year closed with generally below-average pressures over the continent during November and December, possibly related to the downward propagation

of the October stratospheric anomaly to the surface in November (Fig. 6.2a). Marked circulation anomalies included a strong negative-pressure anomaly over the Peninsula and Weddell Sea region (Relay Station AWS set a new record low monthly pressure for November and Esperanza set a new record low monthly pressure for December); a positive pressure anomaly in the Indian Ocean; and a strong negative pressure anomaly southwest of Australia (Fig. 6.3e). In December, the combination of the negative pressure anomaly over the Weddell Sea region and the positive pressure anomaly in the Indian Ocean once again produced strong warming across the Antarctic Plateau, with both Amundsen–Scott and Relay Station AWS observing new record high mean temperatures of -23.3°C and -25.7°C , respectively (see Sidebar 6.1).

Several record monthly mean wind speeds were reported in 2018. On the Ross Ice Shelf, Ferrell AWS

observed a record high mean wind speed for October of 8.2 m s^{-1} and Gill AWS experienced record high mean wind speeds for March (5.6 m s^{-1}) and September (6.4 m s^{-1}). In West Antarctica, Byrd AWS reported a record high mean wind speed for October of 11.4 m s^{-1} . On the Antarctic Plateau, Dome C II AWS observed a record low mean wind speed for April (1.9 m s^{-1}) and tied its record high mean wind speed for August (4.3 m s^{-1}). Relay Station AWS reported record high mean wind speeds in August (9.7 m s^{-1}) and December (8.4 m s^{-1}).

c. Net precipitation ($P-E$)—D. H. Bromwich and S.-H. Wang

Precipitation minus evaporation/sublimation ($P-E$) closely approximates the surface mass balance over Antarctica (e.g., Bromwich et al. 2011; Lenaerts and van den Broeke 2012), except for the near coastal areas where wind-driven transport of snow

SIDEBAR 6.1: RECORD-WARM CONDITIONS AT THE SOUTH POLE AND THE UNUSUAL ATMOSPHERIC PATTERNS ASSOCIATED WITH THEM—K. R. CLEM, S. BARREIRA, R. L. FOGT, S. COLWELL, L. M. KELLER, AND M. A. LAZZARA

The high East Antarctic Plateau is the coldest and driest region on the planet. Weather observations in this remote part of the world began in 1957 with the development of two year-round staffed scientific research stations: the United States' Amundsen–Scott Station and Russia's Vostok Station. Amundsen–Scott is located at the geographic South Pole, at an elevation of 2835 m a.s.l.; Vostok is located in the East Antarctic Plateau and is Antarctica's highest staffed weather station at an elevation of 3490 m a.s.l. (see Fig. 6.1 for map). Average winter temperatures at Amundsen–Scott and Vostok range from -60°C to -68°C ; summer temperatures range from -28°C to -32°C . Vostok Station recorded the world's lowest observed air temperature on record (-89.2°C) in July 1983 (Turner et al. 2009), and neither station has ever recorded an above-freezing temperature. Additionally, satellite thermal emission temperatures of higher-elevation areas suggest that surface snow temperatures can plunge to -98°C in winter, with overlying $\sim 2\text{-m}$ air temperatures estimated at -94°C (Scambos et al. 2018).

During 2018, there were several months of highly unusual atmospheric circulation patterns over the plateau that led to the warmest annual mean conditions on record at Amundsen–Scott and Vostok. Both stations reported an annual mean temperature anomaly of $+2.4^{\circ}\text{C}$ above their respective 1981–2010 climatological means. Amundsen–Scott observed a record high annual mean temperature of -47.1°C , and Vostok recorded a record high annual mean temperature of -52.9°C .

Figure SB6.1 shows the monthly mean temperature anomalies for 2018 at Amundsen–Scott and Vostok stations along with the spatial annual mean, May–June, and December surface pressure and surface air temperature anomalies. The year was characterized by a positive pressure anomaly over the plateau and a broad negative pressure anomaly stretching from the Weddell Sea across West Antarctica and into the South Pacific, with positive temperature anomalies of more than $1^{\circ}\text{--}2^{\circ}\text{C}$ seen across much of the East Antarctic coast and high plateau.

Temperatures were near normal in January and February at both stations. In March, an unusual circulation pattern developed that persisted through June, and a similar pattern developed in December (Figs. SB6.1c,d; see Fig. 6.3). During March, temperatures at both stations were 2°C above average and in May temperatures were 6°C above average. Amundsen–Scott recorded its largest monthly mean temperature anomaly of the year in June, at $+7.2^{\circ}\text{C}$ above climatology, tying 2007 for its warmest June on record at -51.7°C . Figure SB6.1c captures the anomalous circulation and temperature pattern during this period. A 6-hPa positive pressure anomaly developed over the northwest plateau in combination with a broad area of anomalous low pressure extending from the Weddell Sea, Antarctic Peninsula, and into the Bellingshausen and Amundsen Seas. This pressure pattern produced anomalous warm northerly flow that extended from the Weddell Sea (Halley Station recorded a $+6^{\circ}\text{C}$ temperature anomaly in June, see Fig. 6.4c) inland across the plateau, cutting across the South Pole,

CONT. SIDEBAR 6.1: **RECORD-WARM CONDITIONS AT THE SOUTH POLE AND THE UNUSUAL ATMOSPHERIC PATTERNS ASSOCIATED WITH THEM**—K. R. CLEM, S. BARREIRA, R. L. FOGT, S. COLWELL, L. M. KELLER, AND M. A. LAZZARA

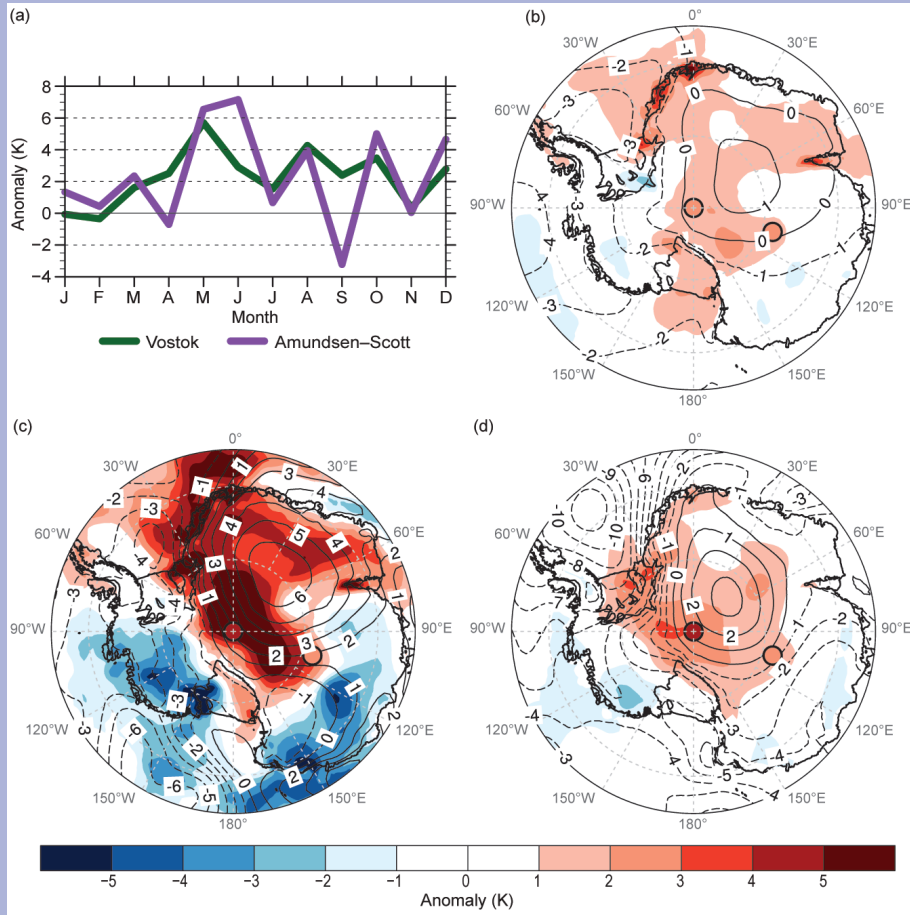


FIG. SB6.1. (a) Monthly mean temperature anomalies at Amundsen–Scott and Vostok stations in 2018 relative to 1981–2010 monthly climatology, and (b)–(d) surface pressure (contours) and 2-m temperature (K, shaded) anomalies relative to 1981–2010 for (b) annual mean, and two periods of exceptional warming across the East Antarctic Plateau, (c) May–Jun and (d) Dec. Amundsen–Scott and Vostok stations are denoted with a circle filled with their respective temperature anomaly. (Source: ERA-Interim reanalysis.)

then descending over the Transantarctic Mountains, leading to anomalous warming on the Ross Ice Shelf. The individual pressure anomalies themselves were not highly unusual, at only ~1 standard deviation from climatology, but their unique alignment and the persistence of this pattern over several months created a favorable fetch of warm flow off the South Atlantic that cut all the way across the continent.

Later in the year, Amundsen–Scott observed its warmest December on record with a monthly mean temperature of -23.3°C , more than 4.5°C above its December climatology and breaking the previous record of -24°C observed in 2005 and 1974. Similar to May and June, the December circulation pattern (Fig. SB6.1d) consisted of a positive pressure anomaly

over the plateau in combination with a strong cyclonic anomaly over the Weddell Sea that extended across West Antarctica and much of the South Pacific. The combined result of these two circulation anomalies was another warm, northerly flow stretching from the Weddell Sea to the South Pole and across much of the high plateau. While the circulation pattern in December was similar to that in May–June, much of the plateau experiences 24 hours of insolation in December. The anomalous subsidence commonly observed with synoptic high-pressure systems likely led to both reduced cloud cover and increased insolation, which in combination with the warm northerly flow, resulted in the warmest December on record at the South Pole.

and meltwater runoff can become significant factors. Precipitation variability is the dominant cause of net $P-E$ changes at regional and larger scales over the Antarctic continent. Precipitation and evaporation fields from the JRA-55 reanalysis (Japanese 55-year Reanalysis; Kobayashi et al. 2015) were examined to assess Antarctic net precipitation ($P-E$) behavior for 2018. (Antarctic $P-E$ from JRA-55 is highly ranked in relation to other global reanalyses (e.g., Liu et al., 2018). Because of the uneven distribution of $P-E$ characteristics (from Peninsula and coastal values $>1000 \text{ mm yr}^{-1}$ to values $<50 \text{ mm yr}^{-1}$ in the East Antarctic interior), annual $P-E$ anomalies relative to a 1981–2010 reference period are presented.

Figure 6.5 shows the JRA-55 2018 and 2017 annual anomalies of $P-E$ (Figs. 6.5a,b) and mean sea level pressure (MSLP; Figs. 6.5c,d). In general, annual $P-E$ anomalies over the high interior of the continent were small (within $\pm 50 \text{ mm yr}^{-1}$); much larger anomalies were observed along the coast, consistent with the low and high net accumulation in these regions. From JRA-55, both 2018 and 2017 – annual anomalies display some spatial similarity over the interior Antarctic continent. The weak 2017 anomalies located along the coast between Queen Maud Land and Mac. Robertson Land (between 5°W and 70°E) were replaced by positive and negative anomaly centers in 2018. The most pronounced positive center was located over Enderby Land ($\sim 45^\circ\text{E}$). Both Queen Mary Land and Wilkes Land (between 90° and 125°E) continued to have strong negative net accumulation anomalies in 2018. These are more extensive than in 2017 and have replaced a small positive anomaly for Princess Elizabeth Land ($\sim 80^\circ\text{E}$) observed in 2017. The weak negative anomalies over Adélie Land and Victoria Land (between 125° and 165°E) became weak positive ones in 2018. The Ross Ice Shelf, which had a positive anomaly in 2017, had a weak negative anomaly in 2018. The Amundsen and Bellingshausen coastal areas, which had small negative anomalies in 2017 (between 150° and 70°W), had the second largest 2018 negative anomalies. The observed dipole anomaly patterns over two sides of the Antarctic Peninsula in 2017 were replaced by positive anomalies, especially on the west side. Weakly negative 2017 anomalies over the Weddell Sea coast were replaced by significantly positive values during 2018.

These annual $P-E$ anomaly features are generally consistent with the mean annual atmospheric circulation implied by the MSLP anomalies (Figs. 6.5c,d). In general, the 2018 annual MSLP anomalies surrounding Antarctica were more regionalized and

of higher amplitude than in 2017, with strong seasonal variations during 2018 (e.g., Fig. 6.3). The observed negative anomalies over the Weddell Sea in late 2017 amplified and expanded, covering most of the Southern Ocean in early 2018 (see Fig. 6.3a). The largest negative anomaly center was in the Bellingshausen Sea (March–May), then later in the Amundsen Sea (June–August), then the Ross Sea (September–November) as the seasons progressed (Figs. 6.3b–e). A secondary negative MSLP anomaly was present along the Antarctic coast between 100° and 165°E through 2018 (Fig. 6.5c). These seasonal variations in MSLP, when annually averaged, resulted in two large negative anomaly centers over the Bellingshausen Sea and near the coast of Adélie Land and a secondary negative anomaly center over the Weddell Sea. The annual negative anomalies produced strong onshore and offshore flows at the Antarctic coast, resulting in large $P-E$ changes in 2018 (Fig. 6.5a): positive anomalies near 150°E , 60°W , and 15°W , and negative anomalies near 105°E and 120°W .

Earlier studies (e.g., Cullather et al. 1998; Tsukernik and Lynch 2013) show that most of the moisture transport into the interior of Antarctica occurs in the West Antarctic sector. Moisture transport shows large interannual variability associated with variations of ENSO (e.g., Bromwich et al. 2004) and SAM (e.g., Fogt et al. 2011). Figure 6.5e shows the time series (with 6-month running means) of monthly total $P-E$ over Marie Byrd Land–Ross Ice Shelf (75° – 90°S , 120°W – 180°) and the monthly Equatorial Southern Oscillation index (EQ-SOI) and SAM indices. The EQ-SOI is used here to represent ENSO events (negative EQ-SOI signifies El Niño events). The EQ-SOI is a standardized sea level pressure difference between the eastern Pacific (5°N – 5°S , 80° – 130°W) and Indonesia (the western Pacific; 5°N – 5°S , 90° – 140°E) and is centered on the equator.

It is clear that the climate patterns indicated by EQ-SOI and SAM were in-phase (simultaneous La Niña and positive SAM) but had opposite behavior to $P-E$ (less total precipitation) in most months from 2010 to early 2011 (Fig. 6.5e). From then until early 2017, EQ-SOI and SAM fluctuated on the time scale of a few months (weakly in-phase fluctuations except for the large out-of-phase fluctuation from late 2014 to early 2016). Thus, during mid-2011 to mid-2017, EQ-SOI and SAM were often offsetting factors modulating precipitation, resulting in little net change in total $P-E$. In late 2017 and early 2018, the EQ-SOI and SAM indices returned to a strong in-phase pattern, and again $P-E$ showed a large decrease.

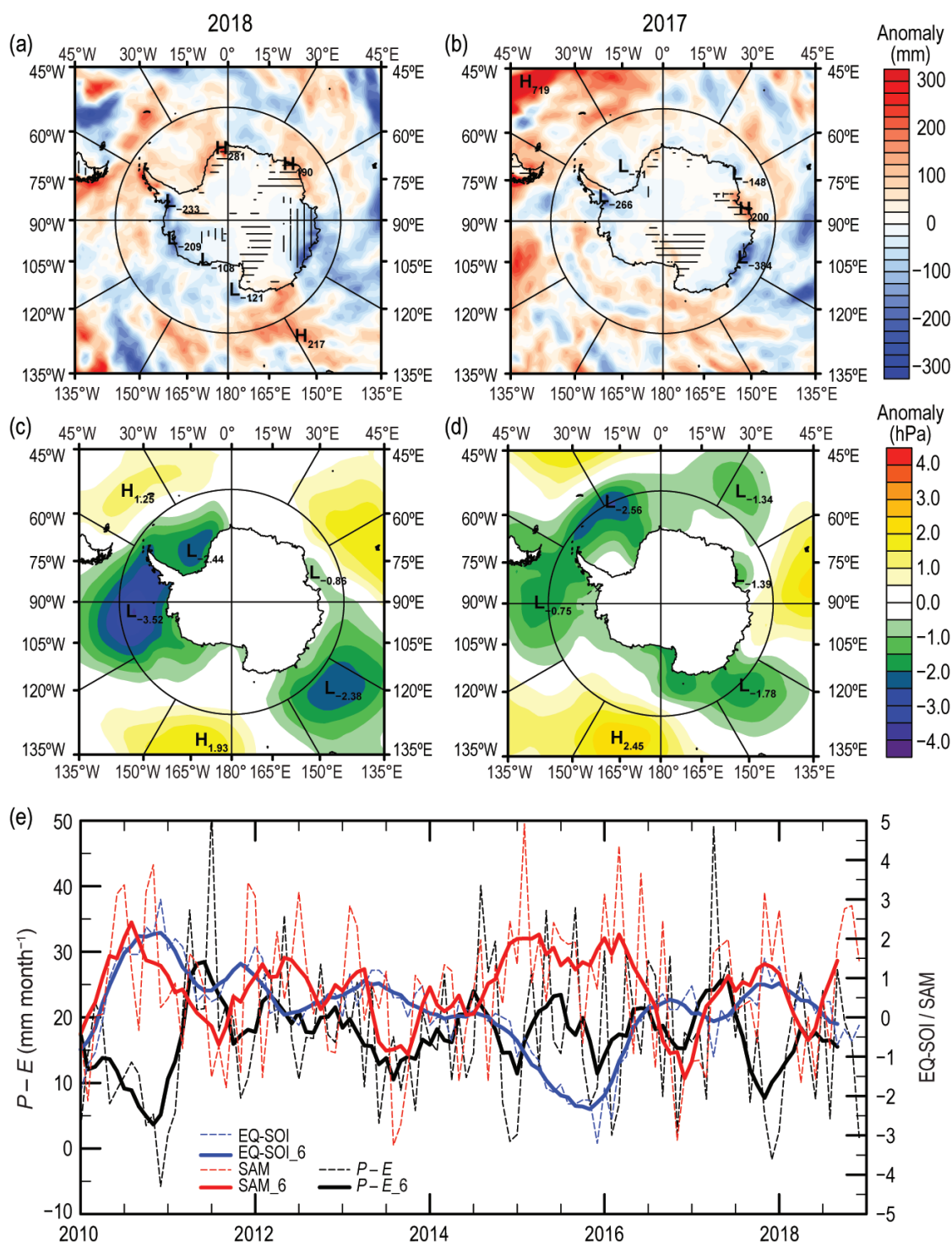


FIG. 6.5. Annual precipitation minus evaporation ($P-E$) and MSLP anomalies: (a) 2018 $P-E$ anomaly (mm); (b) 2017 $P-E$ anomaly (mm). Antarctic regions with $\geq \pm 30\%$ departure from the reference mean are hatched; vertical denotes negative anomaly and horizontal is positive. (c) 2018 MSLP anomaly (hPa); and (d) 2017 MSLP anomaly (hPa). All anomalies are calculated with respect to 1981–2010 means. (e) Monthly total $P-E$ (mm; dashed black) for part of West Antarctica bounded by 75°–90°S, 120°W–180°, along with index trends for EQ-SOI (dashed blue, from NOAA CPC) and SAM (dashed red, from Marshall 2003). Centered 6-month running means are plotted as solid lines.

d. Seasonal melt extent and duration—L. Wang and H. Liu

Patterns in ice sheet surface melt intensity, particularly at the continental ice margins, reflect regional and global climate change and variability. Surface melt intensity is derived from satellite passive microwave data obtained since 1978 and is associated with the number of days above melting temperature (Zwally and Fiegles 1994). Increased surface melt intensity, particularly along the coast, leads to increased percolating melt water and, in extreme cases (unusual in most of Antarctica), melt runoff (Kingslake et al. 2018). The intensity, duration, and spatial extent of surface melt can contribute to the enlargement of ice crevasses (Scambos et al. 2000), accelerated glacier ice flow (Zwally et al. 2002), and disintegration of ice tongues and ice shelves (van den Broeke 2005).

Daily passive microwave brightness temperatures for the 2017/18 austral summer melt season are from the 19 GHz channel of the SSMIS (Special Sensor Microwave Imager Sounder) onboard the DMSP-F17 satellite (ascending passes only). The preprocessed data were obtained from NSIDC as level-3 Equal-Area Scalable Earth Grid (EASE-Grid) format grids (Armstrong et al. 1994) and analyzed using a wavelet transform-based edge detection method (Liu et al. 2005). The first melt event observed after 1 October is the start day of the melt season (Fig. 6.6a), and the last melt event detected is the end day of the melt season (Fig. 6.6b). Melt duration is then the total number of days indicating melt between these two dates (Fig. 6.6c). The duration anomaly map (Fig. 6.6d) was created relative to the 1981–2010 mean melt duration.

Melt extent and melt index (Fig. 6.7) are useful metrics for quantifying the interannual variability in surface melt (Zwally and Fiegles 1994; Liu et al. 2006). Melt extent (in km²) is the total area that experienced surface melt for at least one day during the melt season. Melt index (in day-km²) is the sum of the daily melt extents for Antarctica for the entire season.

Figure 6.6a shows that surface melt first occurred on the Antarctic Peninsula and Wilkins Ice Shelf early in the 2017/18 melt season. However, this initial melting occurred later in the season (November) than is typical for this area (mid-October is common). The continent's melt season ended earlier than in other years (Fig. 6.6b), with only the tip of the Antarctic Peninsula remaining active in March 2018 and other areas ending before February 2018. Ice shelf areas having an extended melt season (>45 day duration, in orange-red) were Larsen, Wilkins, and Shackleton (Fig. 6.6c). Areas with moderate melt duration (green-yellow) included coastal Queen Maud Land and the Abbot and Amery ice shelves. Sporadic short-term melt duration (<16 day, blue color) occurred on the Ross Ice Shelf but with limited areal extent. Compared to 2016/17, the melt area on the Ross Ice Shelf was much smaller.

The melt anomaly map (Fig. 6.6d) shows a generally shorter melt season compared to the historical average. Therefore, austral summer 2017/18 is classified as a low melt year for Antarctica. Three regional exceptions were portions of Queen Maud Land and the northern tip and southwest sectors of the Antarctic Peninsula, which had more than eight days

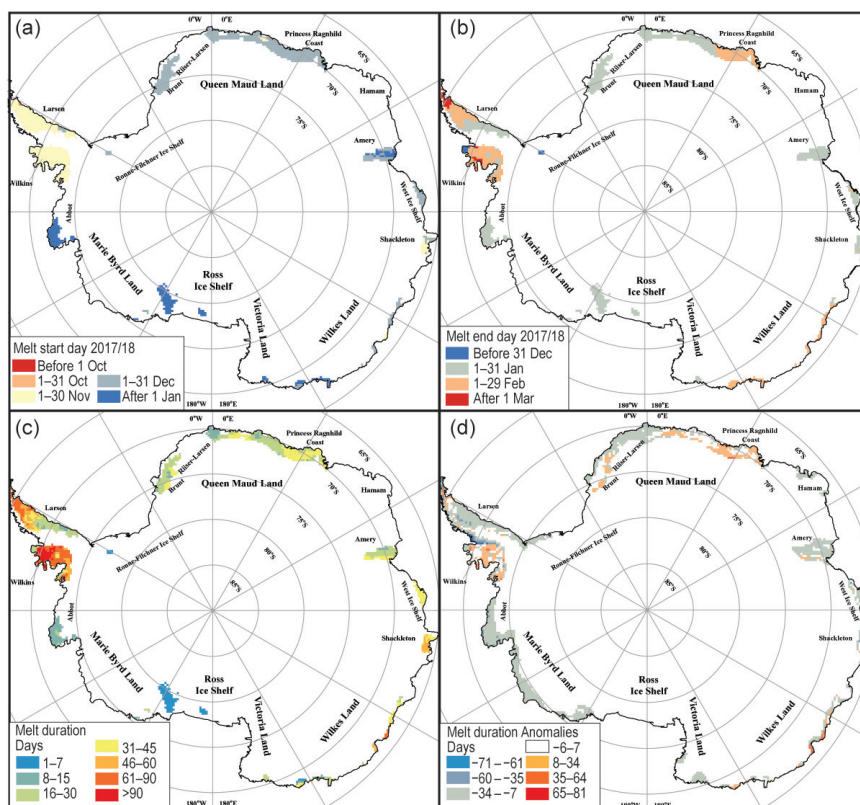


FIG. 6.6. Estimated surface melt for the 2017/18 austral summer: (a) melt start day, (b) melt end day, (c) melt duration (days), and (d) melt duration anomalies (days, 1981–2010 base period).

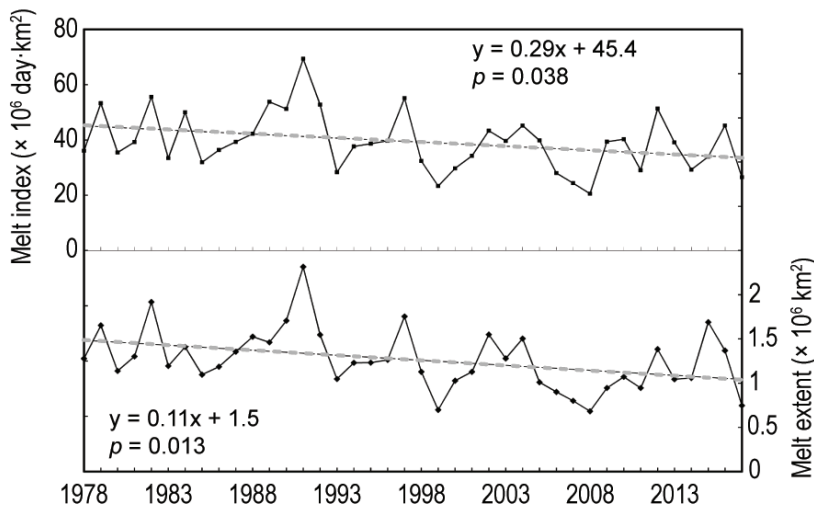


FIG. 6.7. Upper panel: Melt index for Antarctica ($\times 10^6$ day km^2) from 1978/79 to 2017/18, showing a negative trend ($294\,600$ day km^2 yr^{-1} , $p < 0.05$). Lower panel: Melt extent ($\times 10^6$ km^2) from 1978/79 to 2017/18, showing a negative trend ($11\,400$ km^2 yr^{-1} , $p < 0.05$). A record low melt was observed during 2008/09. The year marked on the x-axis corresponds to the start of the austral summer, for example, 2008 corresponds to austral summer of 2008/09.

positive anomaly, coinciding with the positive 2-m temperature anomalies observed in this area during October–December 2017 (Fig. 6.3h in Clem et al. 2018), along with much smaller pockets elsewhere along East Antarctica.

The low melt year of 2017/18 continues a downward trend observed in both melt extent and melt intensity since 1978, trends that are now statistically significant ($p < 0.05$; Fig. 6.7). Since 1978 melt extent has decreased on average $11\,400$ km^2 per year and the melt index by $294\,600$ day- km^2 per year. Year 2017/18 had the third smallest melt extent and fourth lowest melt intensity in the satellite record (1978–present). These observed negative trends are consistent with previous reports (Liu et al. 2006; Tedesco 2009; Tedesco et al. 2009).

e. Sea ice extent, concentration, and seasonality—
P. Reid, S. Stammerjohn, R. A. Massom, S. Barreira, T. Scambos, and J. L. Lieser

Antarctic sea ice plays a pivotal role in the global climate system. Forming a highly-dynamic reflective and insulative blanket that varies seasonally from ~ 3 to $\sim 20 \times 10^6$ km^2 , sea ice and its snow cover strongly modify ocean–atmosphere fluxes and interaction processes (Bourassa et al. 2013). Moreover, brine rejection into the underlying ocean during sea ice formation leads to the generation of Antarctic Bottom Water in areas of high sea ice production that contributes to the global ocean overturning circula-

tion (Johnson 2008). Antarctic sea ice also acts as a protective buffer for ice shelves against potentially destructive ocean swells (Massom et al. 2018) and modulates the interaction of warm deep waters with ice shelf basal cavities to affect melt there (Timmermann and Hellmer 2013; Stewart et al. 2019).

After record high values during 2014, Antarctic sea ice extent exhibited low annual maxima in September 2016, 2017, and 2018. Net sea ice extent has been below the 1981–2010 average since mid-September 2016 (Fig. 6.8a). In 2018, the annual daily minimum (2.15×10^6 km^2) occurred on 18 February, and was the second lowest on record (behind 2017, using the 1979–present satellite mapping). The monthly mean sea ice area for December (5.5×10^6 km^2) was the

lowest for that month ever recorded. Spread throughout the year were 28 days of record low daily sea ice extent and in December alone, 17 days of record low daily sea ice area (Fig. 6.8a).

The persistence of well-below-average total sea ice extent from mid-September 2016 through the end of 2018 suggests that weather systems or atmospheric climate modes cannot fully explain the switch from persistent near-record high (e.g., 2012, 2013, 2014, and 2015 through May) to near-record low sea ice conditions (Fig. 6.8a). Rather, it points to changes in the upper ocean as being a significant contributing factor, particularly in the large basin regions (Section 6f; Lecomte et al. 2017; Swart et al. 2018; Meehl et al. 2019)—with underlying changes, such as warming near-surface waters, inhibiting sea ice growth and/or enhancing melt. However, and as in previous years, large-scale atmospheric patterns were the main factor in causing regional variations and anomalies in the 2018 sea ice coverage.

In terms of broad-scale sea ice behavior, 2018 can be divided into four fairly distinct periods: January–April; May; June to mid-October; and mid-October to December. In mid-summer to mid-autumn (January–April), well-below average net sea ice coverage was dominated by strong negative sea ice extent anomalies in the Ross Sea and central-western Weddell Sea, and latterly the western Amundsen Sea, with lower-magnitude negative anomalies also occurring in the western Pacific sector at $\sim 90^\circ$ – 100° E (Fig. 6.8b).

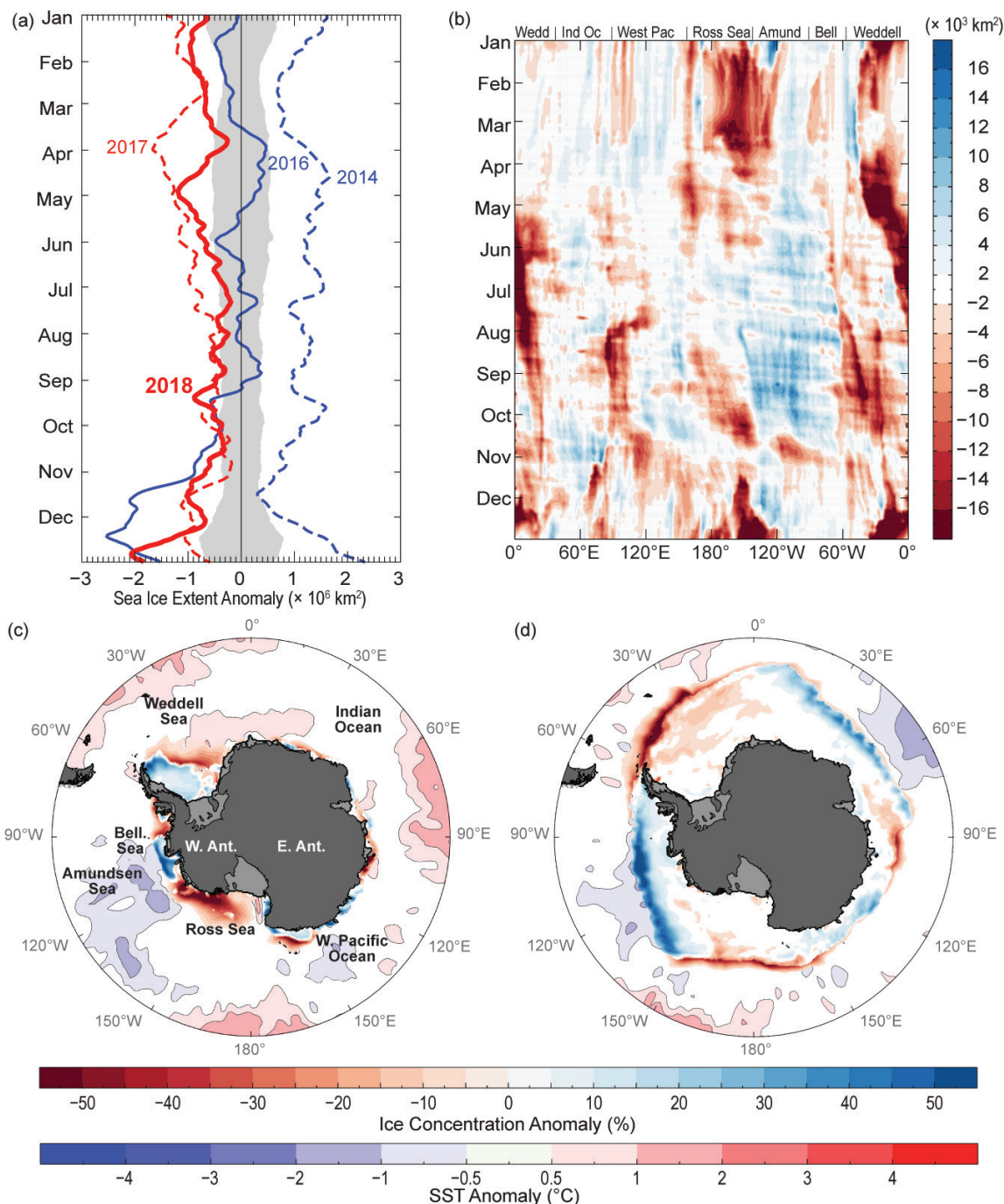


FIG. 6.8. (a) Net sea ice extent anomaly for 2014 (dashed blue line), 2016 (solid blue line), 2017 (dashed red line), and 2018 (solid red line) (from 1981–2010 climatology). The gray shading represents ± 1 std. dev. of extent; (b) Hovmöller plot of sea ice extent anomalies for 2018 (10^3 km^2 per degree of longitude, from the 1981–2010 mean). Maps of sea ice concentration anomaly (%) and SST anomaly ($^\circ\text{C}$; Reynolds et al. 2002; Smith et al. 2008) for (c) Feb and (d) Sep 2018. “Bell.” is Bellingshausen Sea. Based on satellite passive-microwave ice concentration data (Cavalieri et al. 1996, updated yearly, for climatology and Maslanik and Stroeve 1999 for the 2018 sea ice concentrations).

There was relatively extensive sea ice coverage at this time in the $\sim 100^\circ\text{--}140^\circ\text{E}$ region and, notably, in the eastern Amundsen Sea and western Bellingshausen Sea. The relatively high ice concentrations in the West

Antarctic region in particular (Fig. 6.8c) imply wind-driven compaction and/or enhanced freezing due to the presence of colder surface waters. Indeed, below-normal SSTs (e.g., Fig. 6.8c, Fig. 6.10b) and relatively

fresh waters (e.g., Fig. 6.10c) were present adjacent to the ice edge in the Amundsen Sea region, with the former first appearing in September 2017 (see Fig. 6.8d in Reid et al. 2018); this cold pool persisted to the end of 2018.

A change in sea ice coverage occurred during May, with the region of lower-than-normal sea ice extent transitioning from the western to the eastern Weddell Sea in response to a shift in synoptic low-pressure activity from the Amundsen Sea into the Weddell Sea region (e.g., Figs. 6.3a,b). The positive sea ice extent anomaly in the Amundsen Sea expanded into the western Bellingshausen Sea and eastern Ross Sea, while sea ice advance elsewhere was later than normal (Fig. 6.9a).

Following these events and continuing into June, sea ice expansion in the Weddell Sea was slower than average. The negative sea ice extent anomaly in the western Weddell Sea from $\sim 55^{\circ}$ – 5° W displayed an eastward progression (Fig. 6.8b) that mirrors the climatological pattern of zonal sea ice transport from the western to the eastern Weddell Sea from June through November (Kimura and Wakatsuchi 2011). At the same time, there was an eastward progression of a negative sea ice extent anomaly from the eastern Bellingshausen Sea to the west-central Weddell Sea. From June through the end of the year, sea ice extent was also low across the Weddell Sea sector, from $\sim 60^{\circ}$ W eastward to $\sim 30^{\circ}$ E (Fig. 6.8d). The year 2018 saw no reoccurrence of the mid-season Maud Polynya observed in the previous two years (Swart et al. 2018), although several late-season open-ocean polynyas developed in the central Weddell Sea pack ice from late November onward as a result of early sea ice retreat within this region (Fig. 6.9b).

The deep Amundsen Sea low-pressure system that developed in June (Section 6b)

generally persisted through the end of the year. Its presence is likely responsible for the positive anomaly in mid-season ice edge advance over a broad band of the Pacific sector (from $\sim 120^{\circ}$ E eastward to 75° W; Fig. 6.8b, Fig. 6.9a). Another mid-season positive anomaly in ice edge advance was observed across a relatively narrow band in the Indian Ocean sector ($\sim 30^{\circ}$ – 60° E).

Regional sea ice extent (Fig. 6.8b) and seasonal retreat (Fig. 6.9b) were subsequently affected by several variations in the large-scale atmospheric drivers (e.g., as described by Yuan et al. 2018) from mid-October onward (Section 6b; Fig. 6.3b). An atmospheric

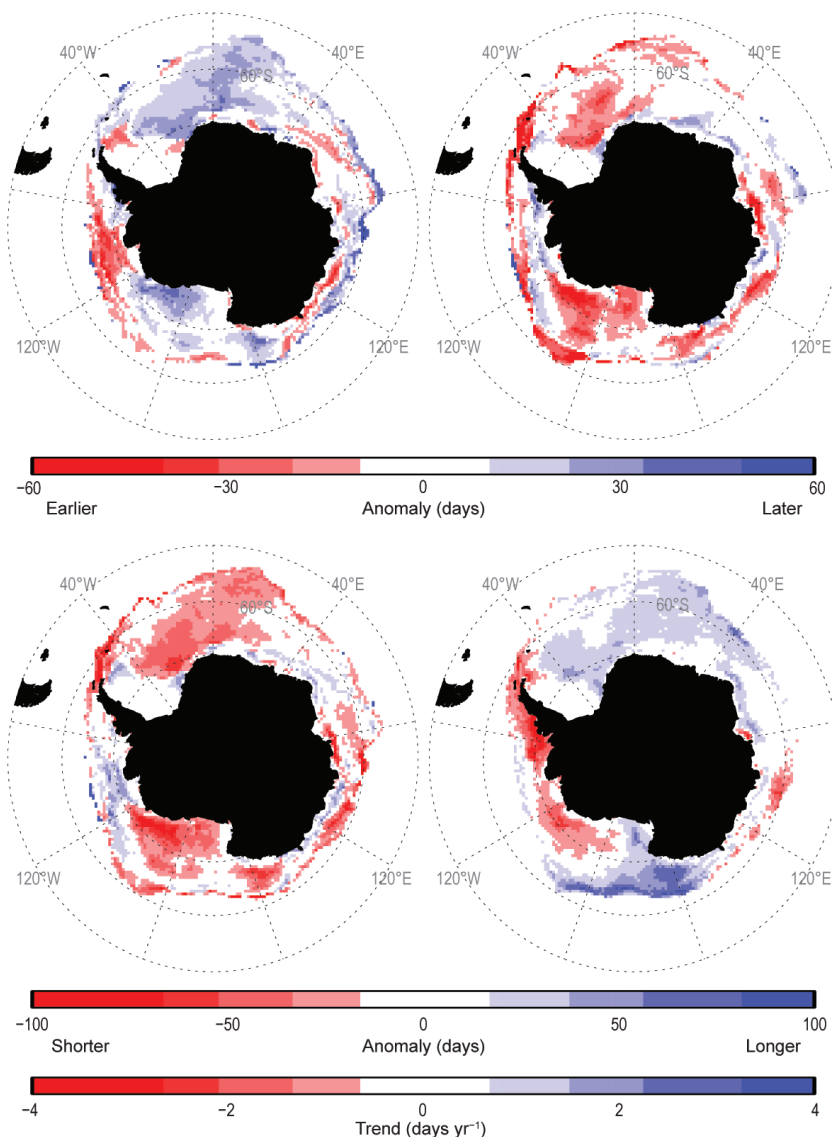


FIG. 6.9. Maps showing anomalies of days of (a) advance, (b) retreat, (c) total duration, and (d) duration trend for the 2018/19 sea ice year (Mar 2018 to Feb 2019). Both the climatology (for computing the anomaly) and trend are based on 1981/82 to 2010/11 data (Cavalieri et al. 1996, updated annually), while the 2018/19 duration-year data are from the NASA Team NRTSI dataset (Maslanik and Stroeve 1999; Stammerjohn et al. 2008).

wave-three pattern developed at that time, with ridges at ~30°E, 160°E, and 60°W, which resulted in early sea ice retreat around most of the continent (Fig. 6.9b) but particularly in the Ross, Weddell, and East Amundsen Seas and the western Pacific sector (generally due to persistent warm northerly winds).

Overall, the below-average sea ice extent within the Weddell Sea and western Ross Sea in 2018 marked a strong departure from positive long-term linear trends in sea ice extent in those two regions (cf. Fig. 6.8b with Fig. 6.9c from Reid et al. 2017). A similar departure is apparent in ice season duration, with anomalously short ice seasons in 2018/19 (March 2018–February 2019) in the Weddell Sea and eastern Ross Sea (Fig. 6.9c) standing in stark contrast to the long-term positive trends observed there (Fig. 6.9d). Likewise, and along most of the western Antarctic Peninsula (~60°–80°W), except the northern tip, the 2018/19 ice season was of average duration, standing in stark contrast to the long-term rapid decreases otherwise observed there. Elsewhere, the 2018/19 ice season duration anomalies (and sea ice extent anomalies from January to mid-May 2018) for (1) the western Amundsen Sea to eastern Ross Sea (120°–160°W) and (2) offshore East Antarctica between ~90°–120°E, are consistent with the long-term trends of shorter ice season duration (Fig. 6.9d) and decreased summer–autumn sea ice extent (see Fig. 6.9c of Reid et al. 2017). However, anomalies in the eastern Amundsen Sea (spanning ~80°–150°W) reflect a recovery in ice edge advance (Fig. 6.9a) and extent, with positive ice season duration and sea ice extent anomalies in 2018 contrasting with regional

long-term trends there (Figs. 6.9c,d; see also Figs. 6.8a and 6.9c in Reid et al. 2017).

f. Southern Ocean—A. Meijers, J.-B. Sallée, A. Grey, K. Johnson, K. Arrigo, S. Swart, B. King, M. Meredith, and M. Mazloff

The Southern Ocean exerts a disproportionate influence on planetary climate due to its central role in the global overturning circulation. Here, strong upwelling, modification, and subduction of water masses result in the uptake of more than 70% and 40% of global ocean anthropogenic heat and carbon, respectively (Frölicher et al. 2015). Despite its importance, it is difficult to evaluate the state of the Southern Ocean in any given year due to the relative sparsity of ocean observations and the short historical time series against which to assess them. Satellite-borne sensors provide comprehensive measurements of the ocean surface, and autonomous instruments are beginning to address the in situ data void (e.g., Newman et al. 2015). Notable amongst the latter are state-of-the-art observations of winter pH that provide new insights into ocean–atmosphere carbon exchange.

1) SURFACE MIXED LAYER PROPERTIES

All available Southern Ocean hydrography data for 2018, including seal tags (MEOP April 2018), Argo floats (updated 15 December 2018), and ship-based hydrographic casts (WOA update, 15 December 2018), were combined into a coherent database comprising 38 970 profiles of temperature and salinity. Anomalies in surface mixed-layer depth (MLD), temperature, and salinity, and their contributions to upper ocean

SIDEBAR 6.2: RECENT DRIFT AND EVOLUTION OF LARGE ICEBERGS IN THE SOUTHERN OCEAN—A. SCARDILLI, F. CLAUS, C. A. SHUMAN, AND T. SCAMBOS

Tabular icebergs are almost unique to the Southern Ocean because they originate from large ice shelves or ice tongues that are now nearly absent in the Northern Hemisphere. Their evolution from calving to drift to eventual disintegration illustrates many interesting aspects of both glaciology and oceanography. Several events in 2018 highlighted these iceberg processes (Figs. SB6.2a–d).

In July 2018, reports from commercial ships crossing the far southern Atlantic Ocean and Argentine Sea described several large icebergs farther north than typically encountered. Tabular icebergs generally remain south of 52°S (Budge and Long 2018), but reports of icebergs north of 45°S, and, by September, as far north as 37°S, indicated an unusual tabular iceberg drift path. In July, ice analysts at Argentina's Naval Hydrographic Service began tracking several icebergs using satellite imagery, looking back through the

record for the origins of reported iceberg swarms and watching their ongoing drift, while continuing to collect ship reports. In total, approximately 25 icebergs >1 km in length were identified in several regions between the Malvinas Islands (Falkland Islands), south Georgia, and Mar del Plata (Fig. SB6.2, bottom). As a result, the maximum northern limit of iceberg drift was extended by the Hydrographic Service.

The origin of the iceberg swarms is likely the breakup of several larger icebergs near the northern tip of the Antarctic Peninsula beginning in May 2018, among them icebergs B09F, B-15T, B-15Z, and A-57A. Several of these icebergs disintegrated as they reached lower latitudes (Figs. SB6.2b,d). These ruptures, or disintegration events, generated dozens of smaller icebergs that then drifted northward and northeastward.

stability were computed relative to the climatological (2000–10) seasonal cycle (Figs. 6.10a–e). In 2018, the MLD was up to 100 m deeper than average in the Pacific east of 120°W. This contrasts with the west Pacific MLD where there was a trend toward net shoaling. The split across the Pacific MLDs appears to be driven by mixed-layer temperatures that were anomalously high in the west and low in the east, with respective increases and decreases in vertical stability (Fig. 6.10d). Such a mode of variability in the South Pacific was observed by Cerovečki et al. (2019 in press), who suggest it may be wind-driven and related to the relative phases of the SAM and ENSO atmospheric modes. The 2018 Southern Ocean temperature anomaly exhibited an almost identically opposite quadrupole pattern to that observed in 2016 (Mazloff et al. 2017). In 2016, both SAM and ENSO were strongly positive, whereas SAM and ENSO were largely out of phase and weak over most of 2018 (after a period of in-phase condition early in the year; Fig. 6.5e; note that SOI and ENSO indices have opposite sign for El Niño and La Niña). Elsewhere, there was weak MLD shoaling in the Atlantic sector associated with strong mixed-layer warming of up to 2.5°C north of the polar front, contrasting with strong cold anomalies seen in this same sector in 2017 (Swart et al. 2018).

South of the polar front there was a consistent circumpolar deepening of the MLD in 2018, which appears to be associated with an increase in salinity. This increased salinity may be due to enhanced entrainment from below by the deeper mixed layers or reduced freshwater export by the largely reduced sea ice extent in 2018 (Section 6e, Fig. 6.9c). The increase in salinity is particularly strong in the Pacific sector and extends farther to the east than a similar positive salinity anomaly seen in 2017, suggesting a possible advective influence. This salinification also contributed to a reduction in the stability of the upper ocean north of the sea ice edge in the Ross Sea sector, as well as farther north in the Tasman Sea and western Pacific (Fig. 6.10e). The reduced mixed-layer stability over Maud Rise (~66°S, 3°E) is notable given the large open-ocean polynya present there in 2016–17 (Swart et al. 2018), and suggests that it may continue to impact the region despite not appearing in 2018.

2) OCEAN COLOR: PHYTOPLANKTON ABUNDANCE

Phytoplankton abundance, as indicated by chlorophyll *a*-concentration, was slightly higher in the 2017/18 growing season (July 2017–June 2018) than the 20-year climatological mean (1998–2018), but well within the bounds of natural variation. This con-

tinues a long-term trend of increasing phytoplankton abundance that has been observed since 1998 (Arrigo et al. 2008). Both the largest decreases and increases in mean surface chlorophyll-*a* in 2017/18 (Fig. 6.10g) relative to the climatological mean (Fig. 6.10f) were observed in the Ross Sea—the decrease on the continental shelf associated with the Ross Sea polynya (where the sea ice edge retreat in 2017/18 was exceptionally early; Reid et al. 2018), and the increase in coastal waters of the eastern and western Ross Sea. This is consistent with the Ross Sea being both highly productive and highly variable. The generally productive coastal polynyas around the Antarctic continent were less productive in 2017/18 compared with the 1998–2018 climatology, likely due to an unusually early spring–summer ice edge retreat in 2017/18 (Reid et al. 2018).

3) AIR–SEA CARBON DIOXIDE FLUXES

Observation-based flux estimates for this critical region have traditionally relied on sparse and seasonally biased shipboard measurements. Autonomous biogeochemical-Argo floats, deployed by the Southern Ocean Carbon and Climate Observations and Modelling (SOCCOM) project, now provide year-round observations of pH, oxygen, nitrate, and ocean optics in the upper 2000 m of the open ocean (Johnson et al. 2017), permitting new estimates of air–sea CO₂ fluxes (Gray et al. 2018). Including 2018, the SOCCOM data span four full years, presenting the first opportunity to examine interannual variability in these flux estimates.

Overall, the Southern Ocean appears to have absorbed more CO₂ in 2018 than the 2015–18 average, with four of five regions showing increased uptake or reduced outgassing (Fig. 6.11). The largest difference occurred in the Subantarctic Zone (SAZ), where substantially more CO₂ uptake occurred in 2018. The strong wintertime outgassing revealed by the float observations in the high-latitude Antarctic Southern Zone (ASZ) during 2015–17 was reduced slightly in 2018. Given that the 2015–17 float-based carbon flux estimates are well outside the range of variability in ship-based estimates (Le Quere et al. 2018; Gray et al. 2018), these results suggest a shift towards increased carbon uptake by the Southern Ocean in 2018, notwithstanding the persistence of strong wintertime outgassing south of the polar front. However, any assessment of interannual variability at present is limited by the number of observations and their spatial and temporal coverage.

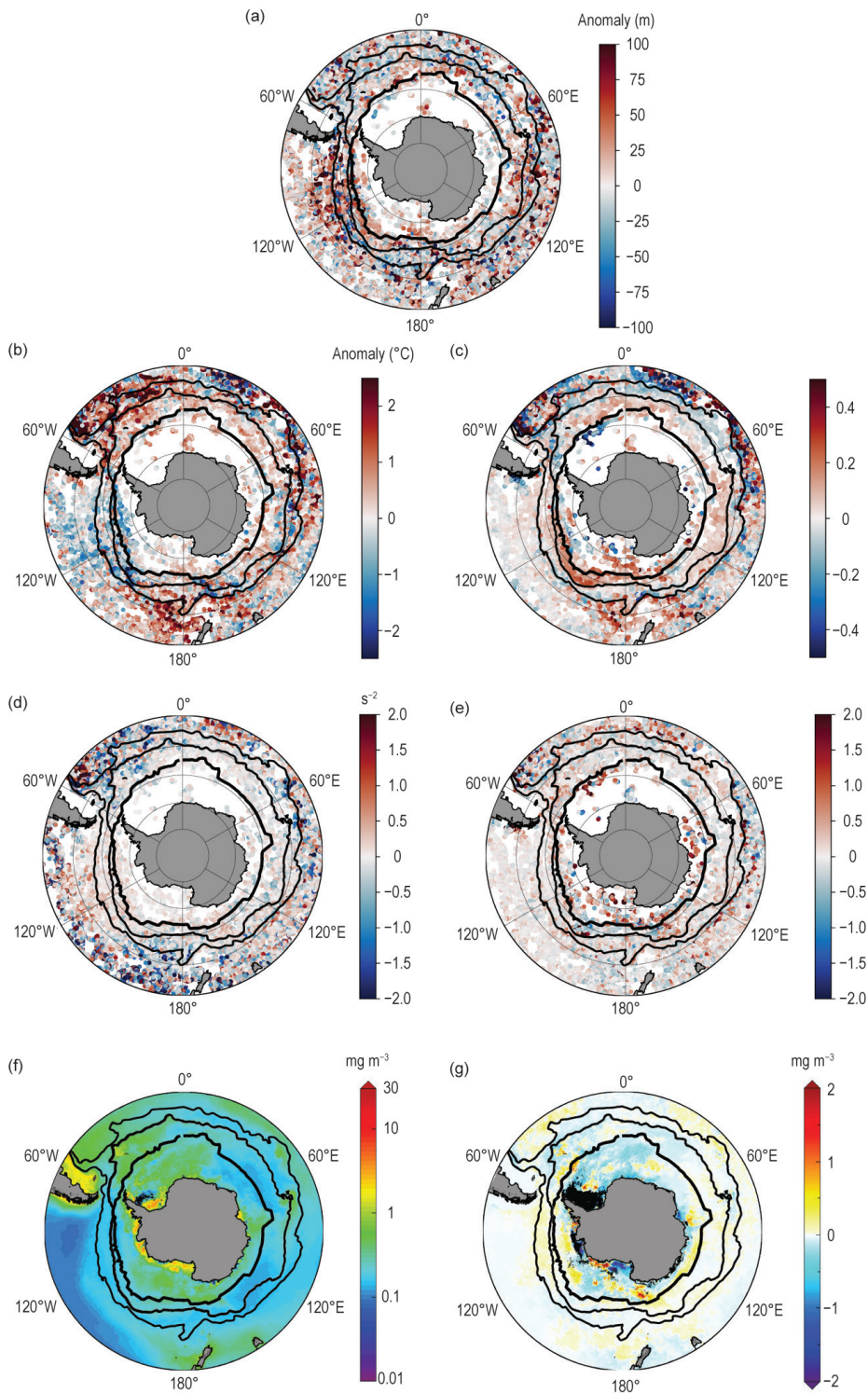


FIG. 6.10. (a) Mixed layer depth anomalies (m) in 2018 from the 2000–10 climatological seasonal cycle. North-to-south, the black contours represent the Subantarctic Front and Polar Front (Kim and Orsi 2014) and the Sep 2018 monthly mean 15% sea ice concentration limit from the NCEP-2 Reanalysis (Kanamitsu et al. 2002). (b) Same as (a) but for mixed layer conservative temperature ($^{\circ}C$). (c) Same as (a) but for mixed layer absolute salinity. (d) Same as (a) but for temperature contribution to stability (N^2) in a 15-m layer immediately below the mixed layer (s^{-2}). (e) Same as for (d) but for salinity contributions. Mixed layer characteristics are computed as in Pellichero et al. (2017). (f) Climatological mean surface chlorophyll-*a* concentration ($mg\ m^{-3}$) for 1998–2018, and (g) anomaly of the austral summer bloom (2017/18) relative to the climatological mean.

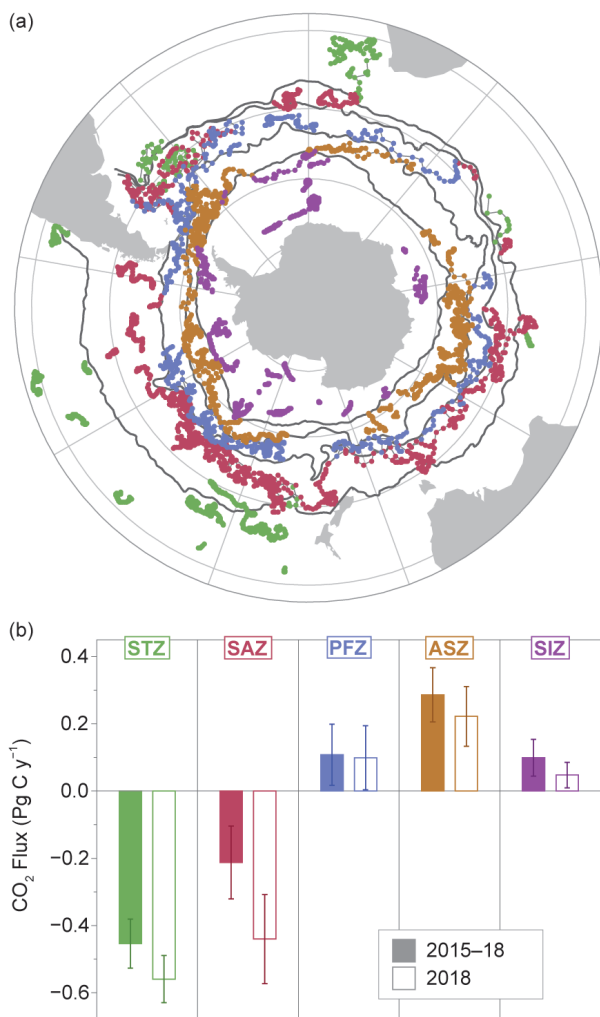


FIG. 6.11. (a) Locations of profiles from SOCCOM floats and (b) average air-sea carbon dioxide fluxes (Pg C yr⁻¹) computed for five regions in the Southern Ocean (STZ = Subtropical Zone, SAZ = Subantarctic Zone, PFZ = Polar Frontal Zone, ASZ = Antarctic Southern Zone, SIZ = Sea Ice Zone). Positive values indicate flux from the ocean to the atmosphere. Carbon fluxes were estimated from float data together with ERA5 reanalysis wind speed and sea level pressure fields, Cape Grim atmospheric CO₂ measurements, and NOAA CDR/NIMBUS near-real-time sea ice estimates following Gray et al. 2018. Solid bars provide the float-based estimates averaged for 1 Jan 2015–31 Dec 2018; open bars correspond to 1 Jan 2018–31 Dec 2018.

g. 2018 Antarctic ozone hole—N. Kramarova, P. A. Newman, E. R. Nash, S. E. Strahan, C. S. Long, B. Johnson, M. Pitts, M. L. Santee, I. Petropavlovskikh, G. O. Braathen, L. Coy, and J. de Laat

The Antarctic ozone hole is a seasonal depletion of the ozone layer over Antarctica occurring every austral spring since the early 1980s. The depletion depends on the amount of ozone depleting sub-

stances (ODS) and the meteorological conditions in the Antarctic lower stratosphere. The structure and evolution of the 2018 Antarctic ozone hole and its relation to previous years were studied using global reanalysis temperatures (from MERRA-2), the NOAA ozonesonde record collected at Amundsen–Scott South Pole Station, satellite observations, and insights derived from a global chemical transport model.

Figure 6.12a shows the 1980–2018 time series of the MERRA-2 reanalysis temperatures at 50 hPa averaged over the polar cap (60°–90°S) during September. In 2018, the mean temperature of the Antarctic lower stratosphere was among the lowest 33% of September mean temperatures observed since 1980. Low temperatures facilitate the formation of polar stratospheric clouds (PSCs), which enable heterogeneous chemical reactions that catalyze ozone loss. The stratospheric wave activity that controls vortex temperature and stability was weaker than average in August and the first half of October and near average in September, resulting in a close-to-average-sized ozone hole (for this century) that persisted until early December. We note that there is good agreement between ECMWF and MERRA-2 temperature records; a small negative bias (~1K) in earlier years before 1999 (not shown) does not change the conclusions reported here.

Satellite observations show that the hole's area, defined as the area where total column ozone values drop below 220 DU, averaged 22.7 million km² (Mkm²) in September 2018, the 15th largest out of 40 years of satellite observations (Fig. 6.12b). Effective equivalent stratospheric chlorine (EESC, an estimator of human-produced and natural ODS in the stratosphere) is shown as a green curve in Fig. 6.12b. The EESC level is estimated employing the method described in Newman et al. (2007), using an updated inventory of near-surface concentrations of ODS gases from ground-based observations and their respective lifetimes. Because of the Montreal Protocol and its amendments, EESC has declined about 11% since its peak in 2000. Reduced ozone depletion over Antarctica due to the EESC decline is more pronounced in September, when catalytic chemical loss is the greatest (Hassler et al. 2011; Strahan and Douglass 2018).

In September, the ozone hole is also strongly affected by meteorological conditions (Fig. 6.12a)—it is larger in colder years and smaller in warmer years. A comparison of years with similar meteorological conditions but different EESC yields a relationship between EESC and ozone hole area of about 125 ppt EESC per Mkm² in the five coldest years since 1984 (Strahan et al. 2014). The 2006 September mean

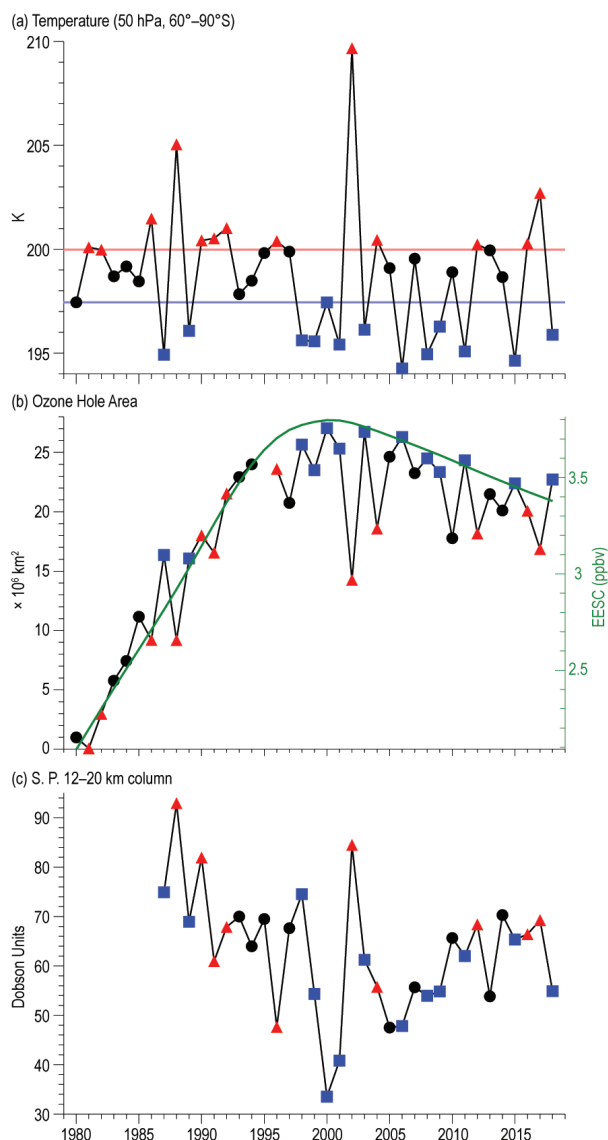


FIG. 6.12. (a) MERRA-2 50-hPa Sep temperature averaged over 60°–90°S, (b) Sep average Antarctic ozone hole area, and (c) Sep average ozone column amounts measured within the primary depletion layer (12–20 km) by NOAA South Pole ozonesondes. Years with temperatures in the lowest (highest) third are shown as blue squares (red triangles). Horizontal blue and red lines indicate 33% and 66% percentiles. The green curve (and right vertical axis) in (b) shows the NASA-estimated EESC level in the Antarctic lower stratosphere modeled with the assumption of a 5.2 mean age of air. Ozone data in (b) for 1979–92 are from TOMS Nimbus-7, 1993–94 are from TOMS Meteor-3, 1996–2004 are from EPTOMS, 2005–15 are from *Aura* OMI, and 2015–18 are from SNPP OMPS. There were no satellite total ozone observations for 1995.

temperature was ~1.6 K lower than that in 2018 and its EESC level (3.69 ppbv) was 0.31 ppbv higher than in 2018. The September 2006 mean area was 26.3

Mkm² (third largest on record), and the September 2018 mean area was 22.7 Mkm². The loss of -0.31 ppbv over 12 years, with the sensitivity estimate and the reduction in hole size, yields a downward trend of -0.21 Mkm² yr⁻¹. Analysis during the ozone recovery period (post-2000) in Fig. 6.12b indicates a downward trend of -0.22 ± 0.15 Mkm² yr⁻¹; the trend in the cold years alone is remarkably similar, -0.25 ± 0.05 Mkm² yr⁻¹.

Ozonesondes are regularly launched from South Pole station to monitor ozone vertical distributions. The largest photochemical ozone depletion associated with EESC occurs in the lower stratosphere between 12 and 20 km (Fig. 6.12c). Below-average temperatures in 2018 led to increased ozone depletion, reducing the minimum column ozone amount in the 12–20 km layer (54.9 DU, the lowest since 2013). The column ozone minimum value was 47.8 DU in 2006, when the EESC level was close to its peak.

In 2018, satellite observations of chlorine compounds over Antarctica also showed slightly lower levels than in previous years. Figure 6.13 shows the seasonal evolution of stratospheric chlorine (HCl and ClO), ozone, and PSC volume derived from the NASA MLS and the CALIPSO sensors. Low Antarctic temperatures during polar night lead to PSC formation (Fig. 6.13d); hydrogen chloride (HCl; Fig. 6.13a) reacts with chlorine nitrate (ClONO₂) on the PSC particle surfaces to form Cl₂. This process causes HCl to decline during the austral winter (Fig. 6.13a). Subsequently, Cl₂ is photolyzed as the sun returns in August and September, leading to an increase of ozone-reactive ClO, whose concentration peaks in September (Fig. 6.13b). The presence of ClO is evidence of ongoing catalytic ozone depletion, and ozone concentration reaches its minimum in late September (Fig. 6.13c). MLS measurements show that chlorine levels (Figs. 6.13a–b) in September 2018 (red) were below the 2005–17 average and notably lower than in 2006 (blue). The vortex average ozone concentration in the lower stratosphere (Fig. 6.13c) in September 2018 (red) was close to the 2005–17 average (white) and higher than in 2006 (blue). Direct observations of PSCs from CALIPSO indicate a high volume of PSC during the 2006 (blue) and 2018 (red) winters, which is consistent with below-average temperatures observed in those years. There is a gap in CALIPSO measurements in mid-September 2018—the key month for ozone depletion—but the volume of PSC in the beginning and end of September was close to or slightly above average. These results suggest that higher September ozone abundances in 2018 compared to 2006 were due to reduced EESC levels.

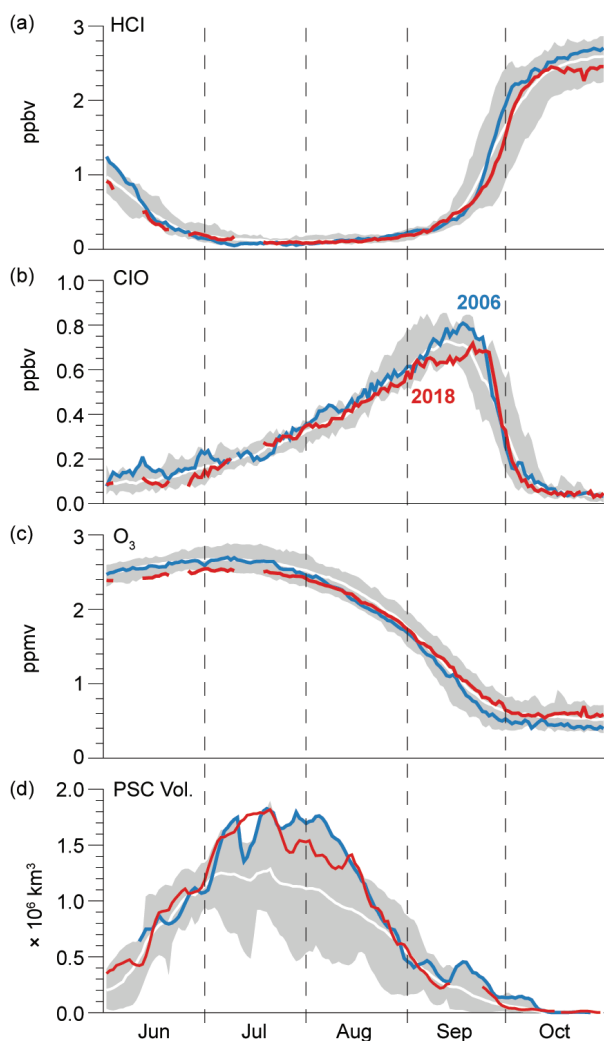


FIG. 6.13. Antarctic 2018 (red curves) and 2006 (blue curves) vortex-averaged concentrations of (a) HCl, (b) ClO, and (c) O₃ from *Aura* MLS (updated from Manney et al. 2011). MLS averages are made inside the polar vortex on the 440-K potential temperature surface (~19 km or 60 hPa). Gray shading shows the range of daily Antarctic values for 2005–17. (d) *CALIPSO* PSC volume (updated from Pitts et al. 2009). Gray shading is for 2006–17.

The NASA Global Modeling Initiative (GMI) chemistry transport model simulates stratospheric ozone and its response to changing EESC levels (Strahan et al. 2013). A model simulation with ozone-depleting source gases held constant at their maximum observed surface levels (1995) produced an ozone hole more than 4 Mkm² larger than a simulation with 2018 EESC levels (Fig. 6.14). The model simulations are driven by MERRA-2 assimilated temperatures and winds, and the simulation with realistically varying ODS levels reproduces the trend and year-to-year variations in Antarctic September ozone from the

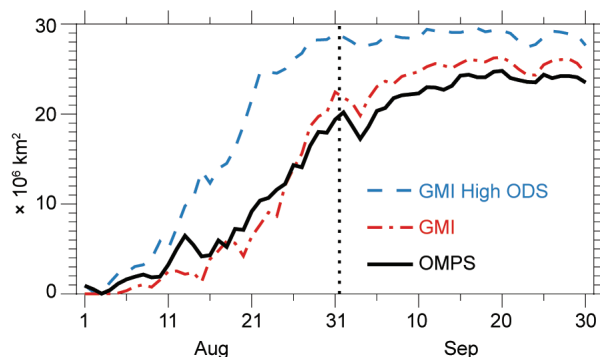


FIG. 6.14. Seasonal evolution of the area of the 2018 ozone hole from *Suomi* NPP OMPS observations (black). Red and blue curves show the area of the 2018 ozone hole from model simulations for two scenarios of the EESC level: with the actual EESC level (red) and with fixed high EESC (blue). The model 210 DU contours are used to account for a 10 DU low bias.

1980s to the present. This simulation has a consistent ~10 DU low bias over the Antarctic in September, accounted for in Fig. 6.14. The 4 Mkm² difference in the September 2018 ozone hole areas in the two GMI simulations indicates a mean area change of -0.22 Mkm² yr⁻¹ over the 2000–18 period.

The 2018 Antarctic ozone hole was near average in size for this century despite below-average temperatures and a stable polar vortex. Comparisons between 2018 and 2006 observations, analysis of ozone hole area trends, and agreement among model simulations all suggest that the 2018 Antarctic ozone hole size and severity were consistent with the expected recovery due to declining EESC.

